

Tuning single-electron charging and interactions between compressible Landau level islands in graphene

Daniel Walkup,^{1,2,*} Fereshte Ghahari,^{1,2,*} Christopher Gutiérrez,^{1,2,*†} Kenji Watanabe,³ Takashi Taniguchi,³ Nikolai B. Zhitenev,¹ and Joseph A. Stroscio^{1,‡}

¹Physical Measurement Laboratory, National Institute of Standards and Technology, Gaithersburg, Maryland 20899, USA

²Maryland NanoCenter, University of Maryland, College Park, Maryland 20742, USA

³National Institute for Materials Science, Tsukuba, Ibaraki 305-0044, Japan



(Received 1 October 2019; published 29 January 2020)

Interacting and tunable quantum dots (QDs) have been extensively exploited in condensed matter physics and quantum information science. Using a low-temperature scanning tunneling microscope (STM), we both create and directly image a new type of coupled QD system in graphene, a highly interacting quantum relativistic system with tunable density. Using detailed scanning tunneling spectroscopy (STS) measurements, we show that Landau quantization inside a potential well enables novel electron confinement via the incompressible strips between partially filled Landau levels (LLs), forming isolated and concentric LL QDs. By changing the charge density and the magnetic field we can tune continuously between single- and double-concentric LL QD systems within the same potential well. In the concentric QD regime, single-electron charging peaks of the two dots intersect, displaying a characteristic avoidance pattern. At moderate fields, we observe an unconventional avoidance pattern that differs significantly from that observed in capacitively coupled double-QD systems. We find that we can reproduce in detail this anomalous avoidance pattern within the framework of the electrostatic double-QD model by replacing the capacitive interdot coupling with a phenomenological charge-counting system in which charges in the inner concentric dot are counted in the total charge of both islands. The emergence of such strange forms of interdot coupling in a single potential well, together with the ease of producing such charge pockets in graphene and other two-dimensional (2D) materials, reveals an intriguing testbed for the confinement of 2D electrons in customizable potentials.

DOI: [10.1103/PhysRevB.101.035428](https://doi.org/10.1103/PhysRevB.101.035428)

I. INTRODUCTION

In a quantum dot (QD), electrons are confined in all spatial dimensions using geometric constraints or a combination of electric and magnetic fields. A tunable quantum workbench, QDs have found a ubiquity of applications. Behaving as artificial atoms [1,2], they are extensively used as tools for emulating basic models of condensed-matter physics [3]. Interacting QDs, and double QDs in particular, are specifically explored as qubits in quantum information technologies [4,5]. First, a double QD can be tuned into various charge configurations controlled by potentials of gate electrodes. The states with near-degeneracy of multiple charge configurations are used for exquisite manipulations of the wave-function dynamics. Second, the strength of interaction, or the coupling, between individual QDs is also controllable by the gates.

Historically, QDs have been fabricated in semiconductor systems, taking advantage of energy band gaps and the variety of fabrication technologies which can control confinement on nanometer length scales. By contrast, in two-dimensional (2D) massless Dirac materials such as graphene, confinement

is inhibited by Klein tunneling through electrostatic barriers [6,7], and true confinement emerges only at high magnetic fields [8–10]. Recently, a method was developed to generate nanoscale electrostatic potentials in backgated graphene devices using the tip of a scanning tunneling microscope (STM) to charge impurities in the boron nitride insulator [11]. This has since been used to create potential wells whose electronic confinement properties were investigated using scanning tunneling spectroscopy (STS) at zero [12], weak [13], and intermediate [14] magnetic fields. Large angle scattering circumvents Klein tunneling and gives rise to quasibound resonances in zero magnetic field [12,15], which undergo a discontinuous jump in energy in weak fields due to modulation of the Berry phase with magnetic field [13]. Electron interactions become important at intermediate magnetic field causing the screened confining electrostatic potential to develop a flattened profile that resembles a wedding cake [14]. This structure results in a concentric series of compressible rings inside the confining potential, separated by incompressible strips [14]. At stronger magnetic fields, the tunnel barriers between these rings become important and Coulomb-blockade phenomena are observed in the scanning tunneling spectroscopy (STS) dI/dV signal, indicating the formation of Landau level (LL) QDs. These Coulomb peaks display a rich, tunable phenomenology, interacting with the local density of states traditionally observed by STS, and revealing novel aspects of the QD system under study, which is the subject of this paper.

*These authors contributed equally to this work.

†Present address: Quantum Matter Institute, University of British Columbia, Vancouver, British Columbia V6T 1Z1, Canada.

‡To whom correspondence should be addressed: joseph.stroscio@nist.gov

In the present experiment, the STM tip combines multiple experimental roles being simultaneously transport contact, gate and charge sensor for QD charging events, and the density-of-states probe of a typical STM/STS experiment. First, it is a mobile “transport lead” which can be positioned over any part of the graphene sheet, inside or outside the QD system. This role appears most clearly at low sample bias, where we observe Coulomb diamonds reminiscent of transport through QDs (e.g., Ref. [1]). At higher bias, however, this picture is modified by the fact that the STM current derives from tunneling to all sample states within a window defined by the sample bias [16], which includes states belonging to LLs whose electrons do not form part of the QD. Second, the tip forms a mobile top gate whose position influences the charge state of the QD. Relatedly, it acts as a charge sensor through a mechanism long known in STS measurements of semiconducting systems [10,17–21]: as the tip locally gates a defect (or QD) state to the Fermi level, charging of the defect causes a sudden shift in the density of states under the tip, and a consequent spike in dI/dV , even without any tunneling current through the defect itself. Continuing the comparison with transport studies of QDs, this role is analogous to a capacitive charge sensor, e.g., a point contact fabricated in proximity to a QD. In most of the data shown here the tip is positioned inside the dot, and the same Coulomb peak can be followed from low bias where it forms part of a Coulomb diamond, to high bias where it can be ascribed to such charge sensing.

In graphene, the unequal energy spacing of the Landau levels, and consequent unequal tunnel barriers between corresponding compressible rings, allows us to control the confinement geometry by changing the index of Landau levels crossing the Fermi energy within the potential well. Thus, for a certain range of gate voltages we can observe Coulomb peaks corresponding to single-dot charging, whereas at other gate voltages, where two widely spaced LLs are being filled, we reliably observe double-dot charging patterns with a lattice of avoided crossings characterizing the interaction between the individual QDs. The particular pattern of these anticrossings shows striking and unprecedented features especially for the first few electrons of the inner Landau level at slightly weaker fields, which we can reproduce by a simple but important modification of the standard two-dot electrostatic model [22]. Analyzing why this ubiquitous and qualitatively different anticrossing behavior has not been observed before, we emphasize the novelty of the QD measurements by STM. In previous works on concentric LL quantum dots [23], the dot was contacted externally using transport leads whereas in the present case we have a moveable lead which can be positioned anywhere over the dot. These results show that graphene QDs in high magnetic fields can be used as a novel quantum-relativistic tool box for realizing complex and intriguing aspects of single electron charging effects in confined quantum Hall systems.

II. DESCRIPTION OF THE QD SYSTEMS

The experimental data was obtained from a high-quality monolayer graphene on hexagonal boron nitride (hBN) on a 285 nm SiO₂/Si device (see methods). The devices used for the graphene QDs are shown schematically in Figs. 1(a)

and 1(d), for p-type and n-type confining potentials, respectively. The confining potentials, $V_0(r)$ [Fig. 1(c)], are produced from charged impurities in the hBN insulator created by pulsing a strong electric field over the graphene/hBN heterostructure [11]. The charge impurities in the hBN layer act as a local fixed nanometer-scale gate potential giving rise to a radially symmetric circular pn junction tunable by the back gate [12,13]. We have created and measured both p-type and n-type quantum wells [Figs. 1(a) and 1(d)] using this technique, and we have observed Coulomb blockade features that are fundamentally similar despite the difference in polarity. Our data consists of the scanning tunneling spectroscopy (STS) dI/dV_B signal, where I is the tunneling current and V_B is the sample bias, measured using the lock-in technique. This data is acquired in a multidimensional space consisting of the tip position \mathbf{r} , the backgate voltage V_g , and V_B ; the tip is held at virtual ground.

In the present system, the QD potential is formed from a combination of the fixed charges in the hBN and the (screened) gating potential of the STM tip. The character of the QD system observed within the potential well depends on the gate voltage and on the energy gaps between those LLs which cross the Fermi energy within it. In general, we find that charging effects appear for those pairs of adjacent LLs that are separated by the largest energy gap (for example, $N = 0$ and $N = \pm 1$), regardless of dot polarity. Coulomb blockade effects were generally not observed for other, higher index pairs of LLs which are separated by much smaller energy gaps. This element of tunability is unique to systems with unevenly spaced LLs deriving from steep, nonparabolic bands, such as graphene.

Figures 1(e)–1(h) show the STS dI/dV signal acquired in line spectroscopy measurements through p- and n-type QDs [Figs. 1(e) and 1(f), respectively] and in x - y raster scans at fixed bias [Figs. 1(g) and 1(h), respectively]. In all panels the gate was set within the double-QD regime, where LL(-1) and LL(0) cross E_F within the well [Figs. 1(a) and 1(d)]. In the raster scans the charging features are due to the effect of spatially dependent tip gating and take the form of concentric rings. The two LLs which are being charged each have their own set of concentric rings; charging rings of LL(-1) and LL(0) are indicated by dark and light-gray arrows, respectively. In the n-type dot [Fig. 1(h)] the centers of the two sets of charging rings have spatially separated centers and can be readily distinguished. In the line spectroscopy measurements [Figs. 1(e) and 1(f)], the two sets of charging peaks appear as series of nested quasi-parabolic “U”-shaped curves whose vertical spacing ΔV_B can be used to estimate the charging energy of its respective QD [see Fig. 2 *et seq.*]. Within each potential well the two sets of charging “U”s can be distinguished by their curvature and spatial extent: those belonging to the outer LL(-1) are broader, flatter, and more closely spaced in ΔV_B , while those belonging to the inner LL(0) are steeper and more widely spaced.

Both types of charging curves resemble the features observed in scanning gate microscopy of QD systems [24,25], and can be explained as an induced charge in the QD,

$$\Delta q = C_{\text{tip}}(\mathbf{r})\Delta V_{\text{tip}} \quad , \quad (1)$$

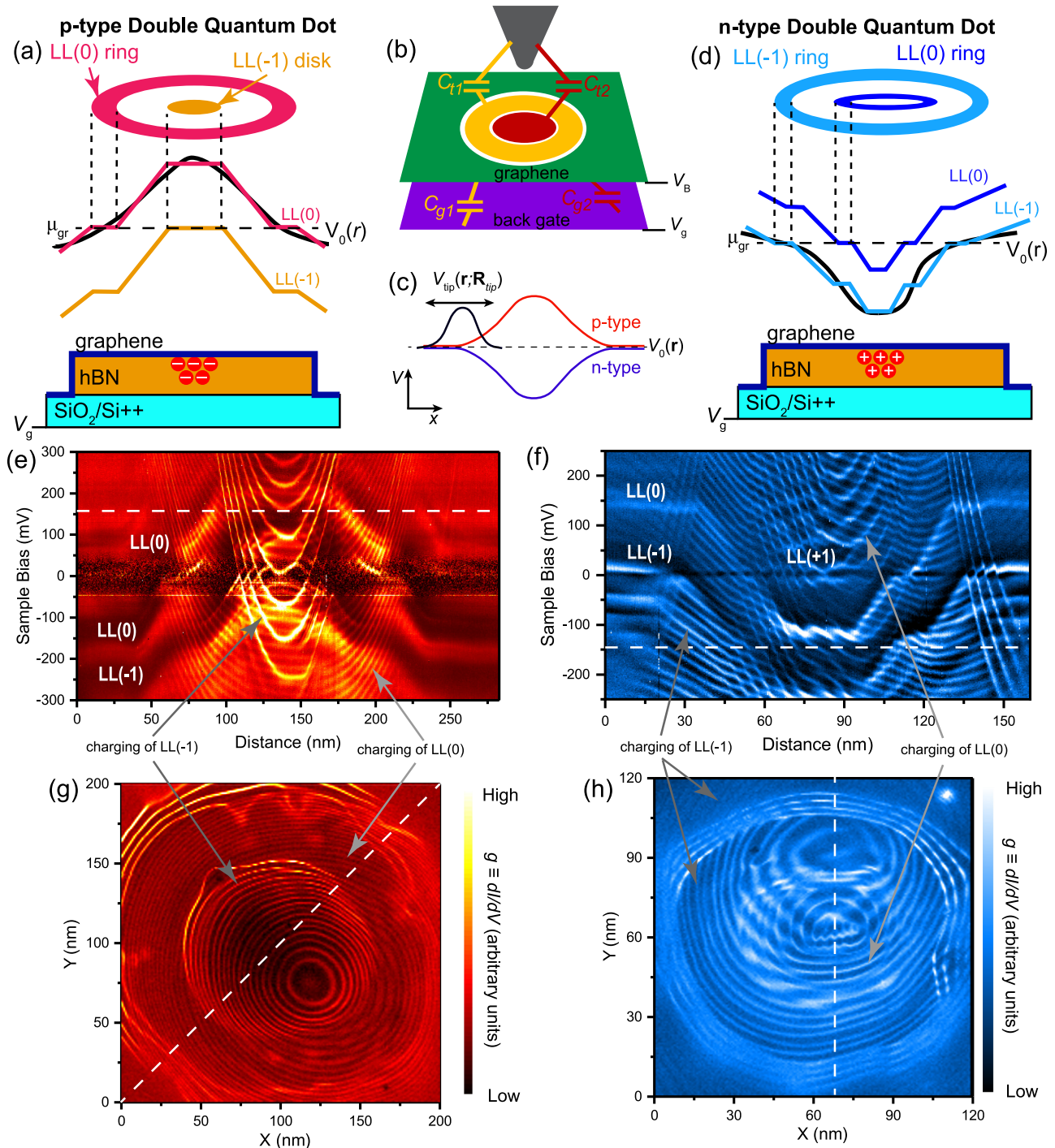


FIG. 1. Real-space imaging of single electron charging of graphene QD compressible islands. Panels (a, d) show cartoons illustrating the Landau level (LL) p-type (a) and n-type (d) QD systems, tuned to the double-dot regime. Both systems are characterized by two LLs crossing the Fermi energy μ_{gr} in a nested pattern, each making a compressible ring or disk. Panel (b) shows the effective capacitances between each LL island and the tip and gate electrodes in the double-dot configuration. Panel (c) shows the different effects of the tip potential on p- and n-type dots: the tip potential tends to reinforce the p-type dot but disrupt the n-type. $g(\mathbf{r}, V_B)$ measurements from p-type and n-type QDs at $B = 8$ T are shown in panels (e, g) and (f, h), respectively. Panels (e) and (f) show energy vs distance tunneling measurements cut through the centers of the QD systems along the dashed white lines in panels (g) and (h), respectively. LLs exhibit plateaus in panels (e) and (f) characteristic of screening, and charging events are observed as series of convex-up parabolas with different curvatures; each panel contains two overlapping sets of curves for the two nested LLs. The same charging features in g as appear as sets of concentric rings in panels (g) and (h). Features associated with the charging of LL(-1) (LL(0)) are indicated by dark gray (light-gray) arrows. Tunneling parameters for (e, g) are $V_B = 300$ mV, $I_s = 100$ pA, and (f, h) are $V_B = 250$ mV, $I_s = 100$ pA, respectively. The reduced intensity near the Fermi level in panel (d) is due to a phonon gap (see Supplemental Material [28] for discussion).

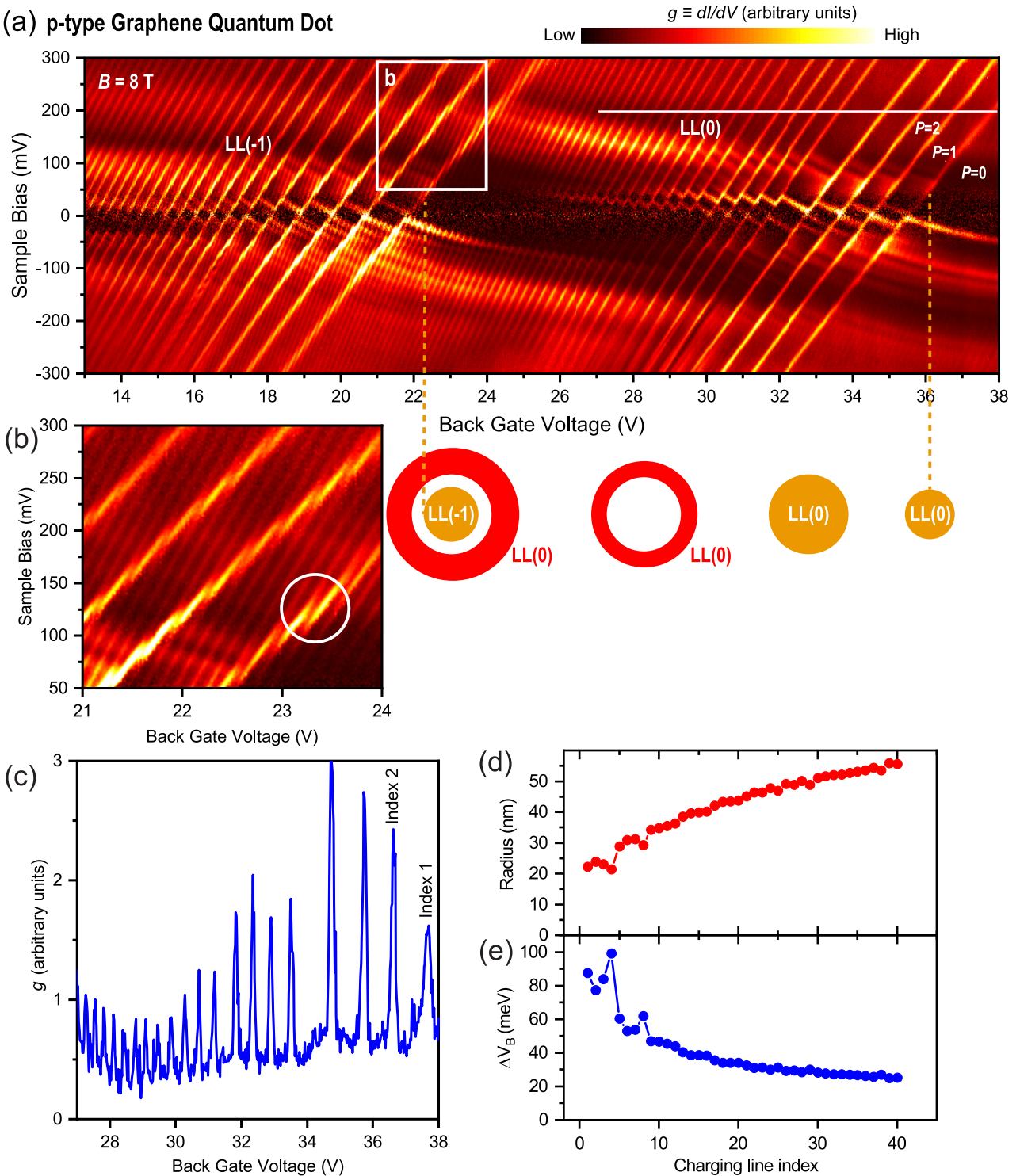
(a) p-type Graphene Quantum Dot

FIG. 2. Mapping of the single charging of compressible rings and disks in p-type graphene QDs. (a) $g(V_g, V_b)$ map with the tip positioned in the center of the QDs for the p-type dot of Figs. 1(a), 1(e), and 1(g) at $B = 8$ T. The rightmost slanted bright line indicates the addition of the first hole to $LL(0)$ at $V_g \approx 36$ V (dashed vertical line). With decreasing gate voltage the $LL(0)$ compressible disk charges and grows in size, becoming a ring when $LL(0)$ is lifted off the Fermi level in the interior of the QD (see schematic below map). At $V_g \approx 22$ V the first hole is added to $LL(-1)$ as it comes to the Fermi level; with decreasing gate voltages both LLs are charged leading to avoided crossings, as shown in (b) [square box in panel (a)] (c) $g(V_g)$ spectrum cut from the dashed horizontal line in panel (a) at $V_b = 180$ mV, showing the charging peaks. (d) The QD radius vs line index, as calculated from the horizontal spacing of the charging lines in panel (a), under the parallel plate approximation where the dot is a conducting disk. Note increasing index corresponds to decreasing gate voltage. (e) The bias voltage spacing of the $LL(-1)$ QD vs line index. The peaks at index four and eight arise from quantum-mechanical energies separating the groups of four charging lines, as shown in panel (c). The statistical uncertainty in panels (d) and (e) is less than the symbol size as determined from the uncertainties in a linear least square fit of the charging lines in panel (a). Tunneling parameters are $V_b = 300$ mV, $I_s = 100$ pA.

where ΔV_{tip} is the contact potential difference between the tip and graphene minus the sample bias V_B . The tip capacitance C_{tip} should be regarded as an effective capacitance that derives from the interaction of the spatially varying tip potential with the QD potential well, as screened by the successive partially filled LL rings. Importantly, since the electron density per filled LL in the quantum Hall regime is fixed, the charging (dis-charging) of the LL quantum dot by the scanning tip is accompanied by growth (shrinkage) of the total occupied area at the Fermi level, and corresponding deformations of the compressible ring which is its boundary.

Since the sample bias V_B represents a tunable offset to ΔV_{tip} , the steepness of the “U”-curves in line STS can be used to estimate the contact potential difference, provided we have a suitable model for the variation of $C_{\text{tip}}(\mathbf{r})$. A rough approximation is found by regarding the double-QD elements as fixed metallic conductors (concentric disk within a ring) and in simulations based on such a model [Fig. S7], a contact potential difference (CPD) of $\approx -0.8\text{V}$ gives reasonable agreement between model and experiment. This estimated CPD agrees well with the work function difference between graphene [26] and Au [27], which comprises the bias contacts of our device, which we used for preparation of the STM tip.

III. EVOLUTION OF THE SYSTEM WITH GATING

A. p-type QD system

Figure 2(a) shows the spectral dI/dV_B gate map as a function of V_B and V_g with the tip positioned in the center of the confining potential. Here, the map is dramatically dominated by slanted bright lines corresponding to adding a single charge to a LL QD, whereas the usual graphene LL LDOS is observed as a nearly horizontal intensity modulation of these features. In Fig. 2(a), a single hole is added to LL(0) starting at a large back gate voltage of $\approx 36\text{V}$, initiating a LL(0) QD disk at the Fermi level. As we decrease the gate voltage, additional holes are added and the dot expands: the filled LL(0) rises above the Fermi energy in the dot center, and the compressible part of this LL expands outward, forming a ring. This increase in dot size is inferred from the closer spacing of the charging lines and confirmed by direct STS measurements [Fig. 1(e)]. At gate voltage $\approx 22\text{V}$, LL(-1) crosses the Fermi level [see schematic below Fig. 2(a)] and a concentric double-QD is formed. This is indicated by a second series of slanted charging lines that are observed together with the original set from the LL(0) QD; the latter are now finely spaced, reflecting the larger size of the LL(0) QD. These two sets of charging lines display an avoided crossing pattern indicative of a double QD [Fig. 2(b)], which is discussed further below.

B. n-type QD system

A similar evolution of the concentric QDs is observed in the n-type confining potential, as observed in Figs. 3(a) and 3(b). The filling of the dot begins with the formation of the LL(-1) disk at gate voltage $\approx -10\text{V}$, and then concentric quantum dots are formed when LL(0) crosses the Fermi level at $\approx 4\text{V}$. This gradual filling process is well-demonstrated in raster scans [Figs. 3(c)–3(j)] and in corresponding line scan

STS data (Fig. S11) which document the growth of the dot with increasing gate voltage. In these scans, the single-dot area can be clearly distinguished as the space circumscribed by a bright halo, inside which the charging lines appear as thin bright rings [Figs. 3(c)–3(e)]. In the STS line-cuts, taken with identical tunneling conditions along a vertical line, this region can be clearly identified with the area in which LL(-1) is below the Fermi energy E_F [Fig. 1(f)]. As the gate voltage is increased the dot area expands taking in more electrons [Figs. 3(c)–3(f)], until LL(0) begins to be filled at the center of the dot. After a brief transition range of gate voltages in which this internal dot is not firmly established for all tip positions [Figs. 3(f) and 3(g)], the raster scans show an internal region in which two sets of charging lines exist [Figs. 3(h)–3(j)]: those corresponding to LL(-1) whose area has expanded significantly, and those of LL(0) which are only visible within the corresponding smaller bright halo. Line spectroscopy [Fig. 1(f) and Fig. S11] shows that this is indeed the zone where LL(0) is below the Fermi level. As compared to the p-type dot [Fig. 1(e)], the raster scans here show a very pronounced asymmetry in the centers of the charging rings, and therefore in $C_{\text{tip}}(\mathbf{r})$ for both dots. We attribute this to a combination of asymmetries of the (unscreened) dot and tip potentials. That the former is somewhat asymmetric can be seen in the line STS measurements, especially Figs. 4(d)–4(f), where, with increasing gate voltage, the expanding LL(-1) is pulled outwards more rapidly on the right side than on the left. (See Supplemental Material [28] for details on the calculation of the $C_{\text{tip}}(\mathbf{r})$ function for an asymmetric tip [Fig. S8], and reference [9] therein.)

When the gate voltage is increased further, a point is reached at which the outer LL, being occupied within the potential well, is pulled below E_F throughout the graphene device. When this happens the “dot” expands to infinity and the LL is not confined anymore. This deconfinement process, or explosion, was observed in the n-type dot [Fig. 4]. Before the explosion, double-dot charging behavior similar to Fig. 3 is observed [Figs. 4(a) and 4(d)]; then as the dot becomes unstable the changes of tip position inherent in scanning are able to disturb the system creating a chaotic picture [Figs. 4(b) and 4(e)]. After the outer dot “explodes,” we recover the single-QD regime where, regardless of tip position, the charging lines vanish and the nearly undisturbed charging pattern of LL(0) remains [Figs. 4(c) and 4(f)].

IV. ELECTROSTATIC MODELLING AND NOVEL AVOIDANCE PATTERN

To interpret and best reproduce the slopes, intercepts, and spacings of the observed charging lines we developed a model incorporating Eq. (1), based on the electrostatic double-dot model formulated for semiconductor QDs [22,29]. In our model the two Coulomb islands are each connected to the back gate and the STM tip by capacitors, but we crucially omit the capacitor *between* the islands: our experimental data requires a new mode of accounting for the interdot coupling, described further on, which is a key result of this work.

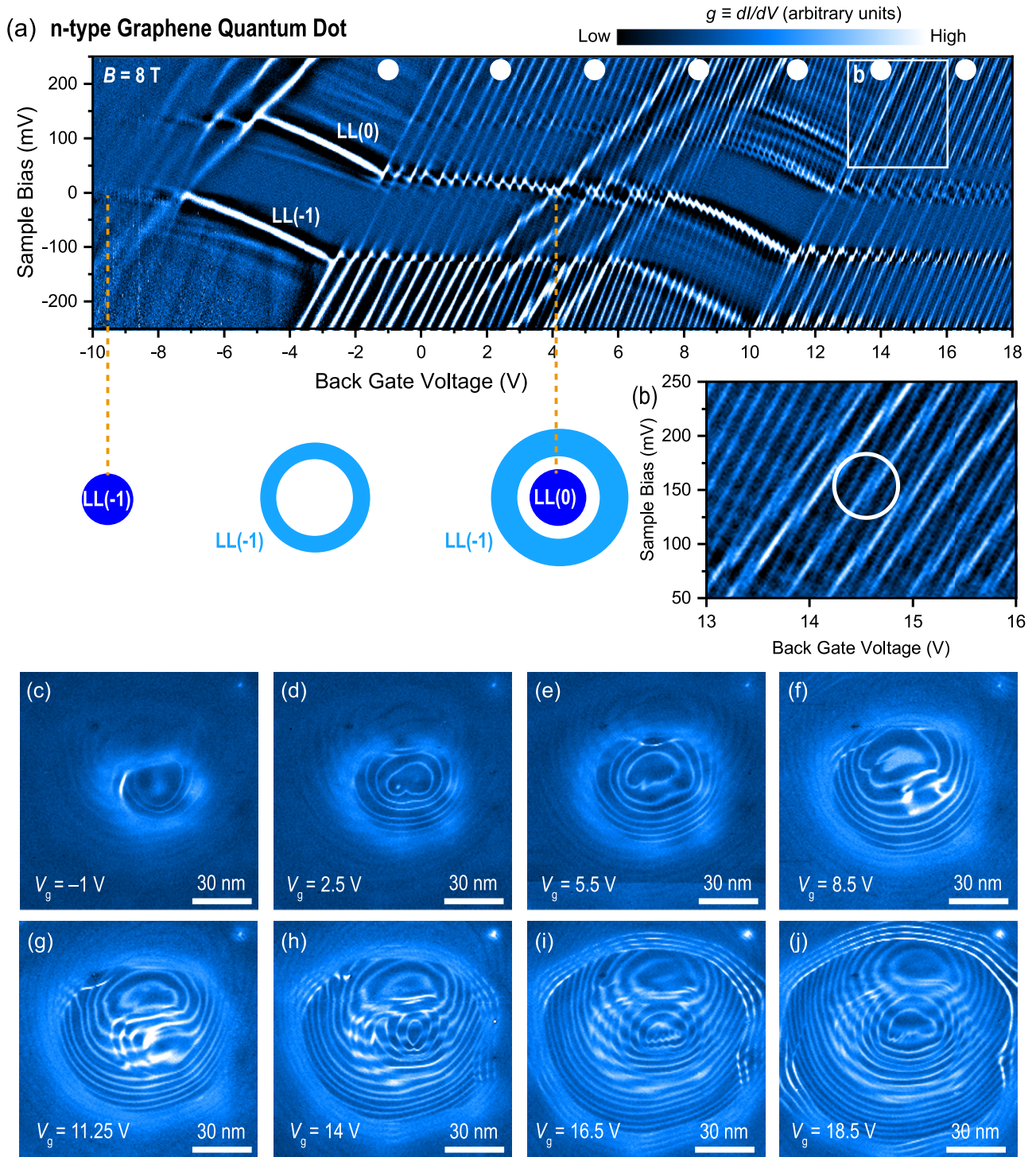


FIG. 3. Mapping of the single charging of compressible rings and disks in n-type graphene QDs. (a) $g(V_g, V_B)$ map with the tip positioned at the center of the QDs for the n-type dot of Figs. 1(f) and 1(h) at $B = 8$ T. At $V_g \approx -9.5$ V the first electron is added to LL(-1) as indicated by the slanted charging line (dashed vertical line). The LL(-1) compressible disk charges and grows in size with increasing gate voltage, becoming a ring when LL(-1) is shifted below the Fermi level (see schematic below map). The second series of charging lines begins at $V_g \approx 4$ V where the first electron is added to LL(0) as it comes to the Fermi level. With increasing gate voltage both LLs are charged and avoided crossings between these charging events are seen in (b), indicated by the square region between $V_g = 13$ V – 16 V. (c–j) $g(\mathbf{r}, V_B = 250$ mV) showing top views of the QD at the indicated gate voltages. The small circles in (a) show the corresponding positions in gate map. With increasing gate voltage, the number of charging lines increases first corresponding to LL(-1) and then LL(0) is seen to start charging in panel (f). Tunneling parameters are the same as Fig. 1(f) and 1(h).

n-type Graphene Quantum Dot Explosion

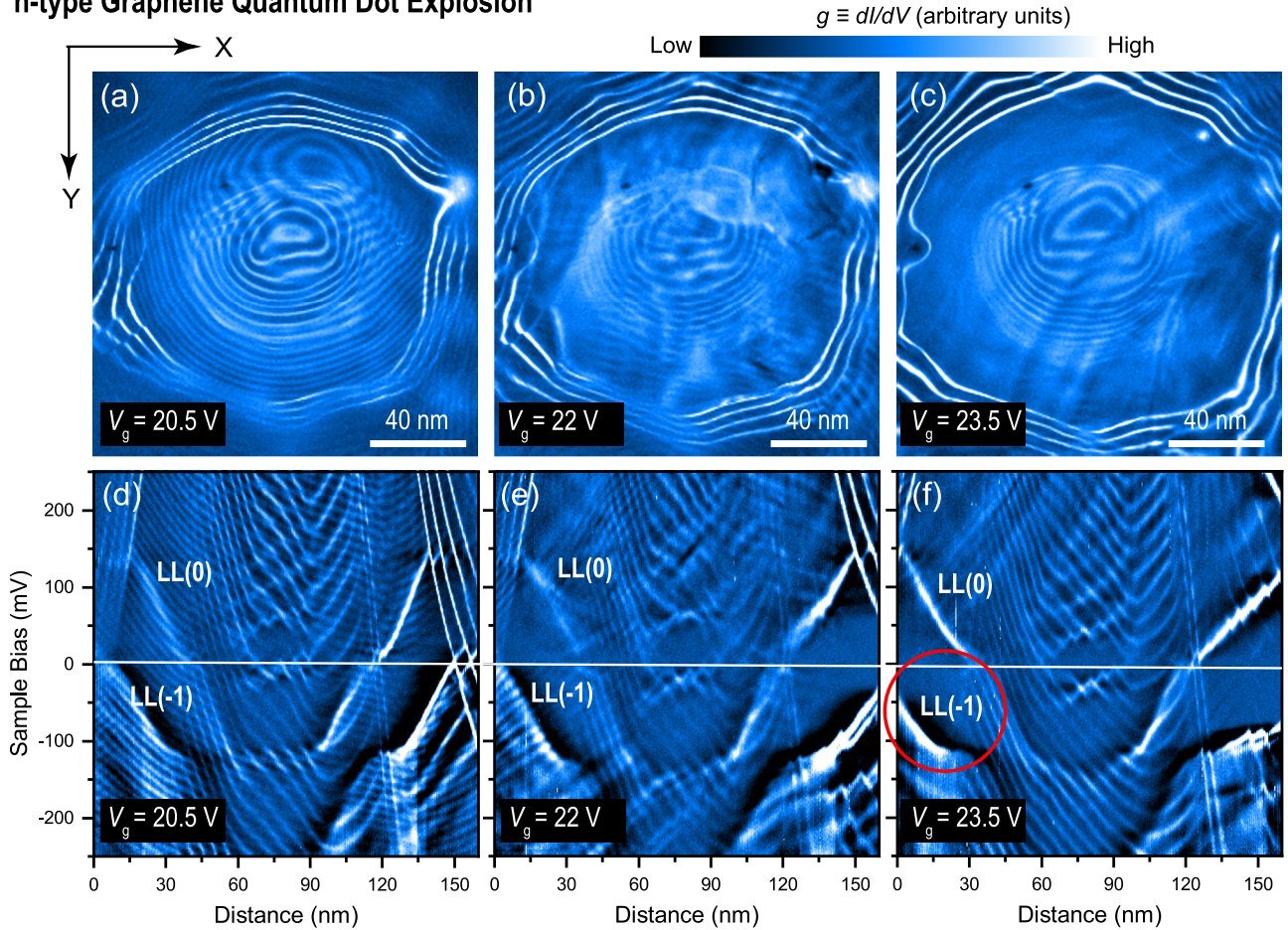


FIG. 4. Graphene quantum dot explosion. $g(\mathbf{r}, V_B)$ measurements of the n-type QD in Figs. 1(d), 1(f), 1(h), and Fig. 3, showing top views in the xy plane (a–c), and corresponding line cuts (d–f) across the centers of the QDs in the sample bias vs. y plane in a narrow back gate voltage range between 20.5 and 23.5 V. In the middle panels (b) and (e) LL(-1) hits the Fermi level at the outer edges of the QD and ceases to be compressible in panels (c, f) when it completely drops below the Fermi level [see red circle in panel (f)]. During this process the $g(\mathbf{r})$ signal becomes highly chaotic until the corresponding charging rings are no longer observed in panel (c). Tunneling parameters are the same as described in the caption of Fig. 3.

The total electrostatic energy of our double-QD system is

$$U(N_1, N_2) = \frac{1}{2} \mathbf{Q}^T \cdot \mathbf{C}^{-1} \cdot \mathbf{Q} = \frac{1}{2} \sum_{i=1}^2 \frac{(N_i e + S_i)^2}{2C_i} \quad (2)$$

where $\mathbf{Q} = (N_1 e \ N_2 e)^T$, \mathbf{C} is the 2×2 capacitance matrix, C_i is the total capacitance of the i th dot, e is the electron charge, and $S_i = C_{gi}(V_g - V_B) + C_{ti}(V_t - V_B)$ is the induced charge on the i th dot from the back gate and tip electrodes, C_{gi} and C_{ti} , respectively, and V_t represents the effective tip potential due to the contact potential difference between tip and graphene. To obtain the last piece of Eq. (2) we assumed that \mathbf{C} has no off-diagonal terms [cf. Eq. (A8) of Ref. [22]].

In this model the charging lines of a single dot (for concreteness, dot 1) have the slope $C_{g1}/(C_{g1} + C_{t1})$, and the spacing of parallel charging lines in the gate direction is $\Delta V_{g1} = e/C_{g1}$, in the absence of a quantum-mechanical energy term. Treating the dot as a conducting disk separated from the back gate by SiO_2/hBN dielectrics, we obtain simple estimates for the dot radius shown in Fig. 2(d). These results agree reasonably well with the experimentally observed dot

sizes [Fig. 1(e)] despite the crudeness of the fixed-conductor approximation. In Fig. 2(e) we plot the bias-voltage spacing ΔV_B of the consecutive charging lines of the single quantum dot. To convert this to the physical addition energy one may either multiply ΔV_B by the tip lever arm (the ratio of the tip capacitance to the total capacitance of the dot), which can be found by independent electrostatic calculations [10], or directly examine the Coulomb diamond features near the Fermi energy; the addition energy is the maximum height of one of its triangles [30]. The lever arm varies systematically with the dot size, and we have omitted the attempt to calculate it precisely. Of special note are the larger gaps between the fourth and fifth and the eighth and ninth charging lines in Fig. 2(c). This reflects the fourfold spin and valley degeneracy of the graphene Dirac states [31]: the discrete Landau level orbital states can each be charged four times, after which it is necessary to overcome an additional energy gap before charging the next orbital. This often leads to a clustering of the charging lines in groups of four. Unequal spacing of charging peaks within the quartet is observed here and elsewhere, and is attributed to lifting of the valley or spin degeneracy [10,32].

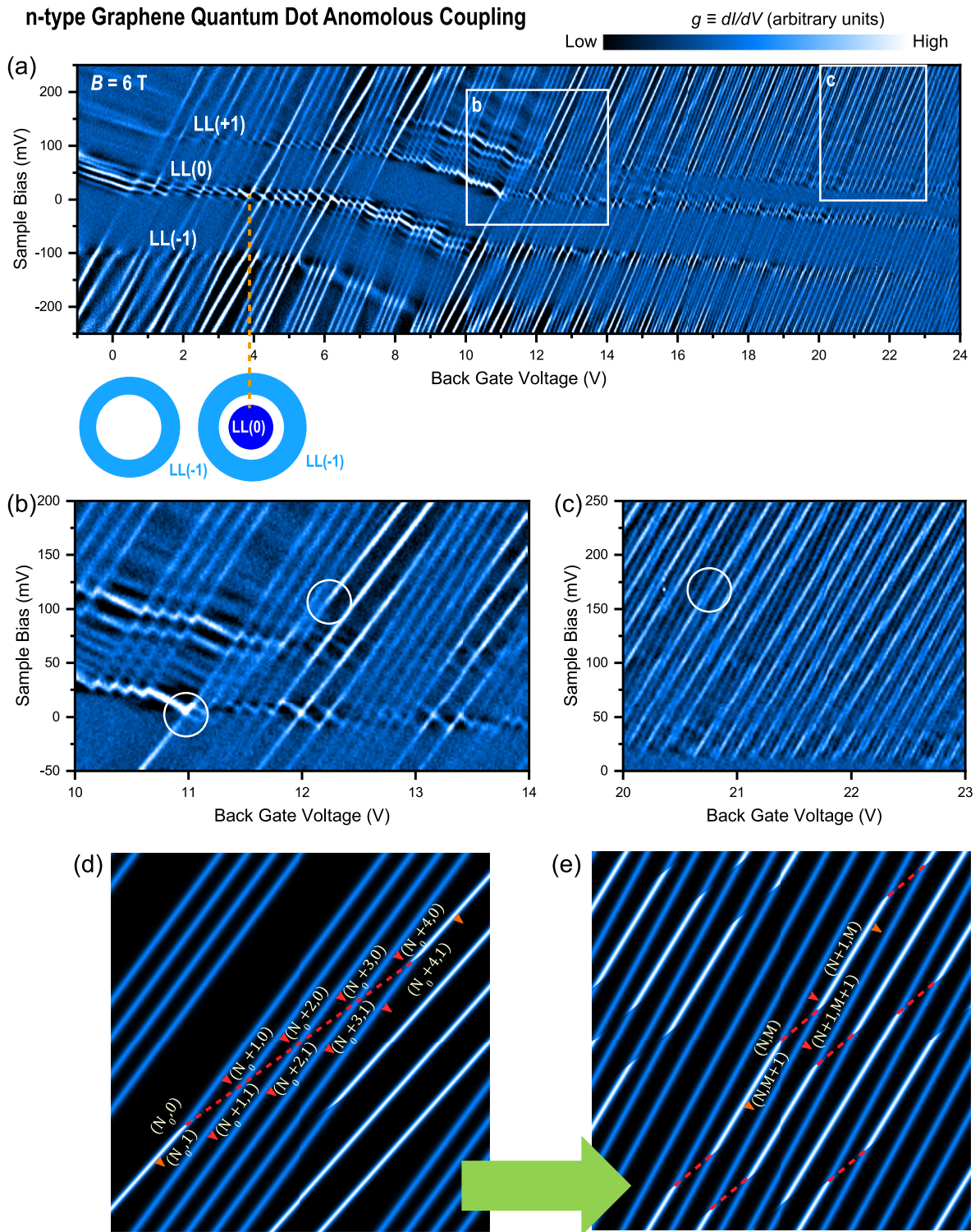


FIG. 5. Tuning the charging and coupling of graphene compressible rings. $g(V_g, V_B)$ map with the tip positioned at the center of the QDs for the n-type QDs of Fig. 2(d) at $B = 6$ T. (a) Large-scale map showing charging lines appearing predominantly in quartets due to the fact that quantum-mechanical energy becoming larger than the charging energy at the lower field of 6 T as compared to Fig. 4(a) at $B = 8$ T. (b) A novel type of avoided crossing is observed at gate voltages below ≈ 18 V with the charging line of LL(0) joining and exiting the quartet of charging lines of LL(-1). (c) The avoided crossing pattern in panel (b) gradually evolves with increased density (gate voltage), into the more standard crossing observed at higher field in Fig. 4. (d, e) Model calculations of avoided crossings observed in panels (b, c), respectively. Within the electrostatic double-dot paradigm, a different charge-counting scheme is required to reproduce the anomalous crossing pattern in panel (b) as discussed in the main text (see Supplemental Material [28] for calculation details and reference [8] therein). Tunneling parameters are the same as described in the caption of Figs. 3.

When two nested dots are being filled, there is a regular grid of avoided crossings [Figs. 2(b), 3(b), and Figs. 5(b) and 5(c)]. We first attempted to numerically simulate the observed avoidance pattern by adjusting the dot-gate capacitances and their mutual capacitance C_m as prescribed in the full double-dot model of Ref. [22]. However, our attempts failed, particularly in describing spectral maps taken in both dots in slightly weaker magnetic fields [Fig. 5]. In the n-type dot measurements at 6 T, the charging lines corresponding to adding the first several electrons to the inner dot show an avoidance pattern highlighted in Fig. 5(b) and schematized in Fig. 5(d), which could not be captured by the standard double dot charging model.

In a typical double-QD system the charge stability diagram is made up of hexagonal cells (Fig. S1), whose boundaries are called charging lines if they represent the transitions $(N_1, N_2) \rightarrow (N_1 \pm 1, N_2)$ or $(N_1, N_2 \pm 1)$, and charge reconfiguration lines if they represent an electron transfer between the dots: $(N_1, N_2) \rightarrow (N_1 \pm 1, N_2 \mp 1)$ [22,33,34]. If we pick a charging line and follow it through the stability diagram, then we find that it executes zigzags as it forms the boundary of successive hexagonal cells. The changes of slope occur at triple points, where three charge states are degenerate. These zigzags are apparent in our gate maps at 8T [white circled regions in Figs. 2(b) and 3(b)].

In our weak-field data, however, the avoidance pattern is fundamentally different: The incoming charging line of the inner dot attaches to a quartet on the lower left and detaches from it on the upper right [Fig. 5(b)]. The charge reconfiguration line, which is shown in red in Fig. 5(d), passes through the quartet without making any zigzags: the charge stability diagram cell is a parallelogram rather than a hexagon. But, increasing the gate voltage in Fig. 5(d) (and thereby enlarging both dots), we find that the zigzags in the outer-dot charging lines begin to reappear, and the hexagonal cell is gradually restored [Figs. 5(a), 5(c), and 5(e)].

In the standard model of QD charging physics, both the limit of large C_m and the increase of the interdot tunnel conductance to $\sim e^2/h$ correspond to an effective merging of the two dots [22,35–37]. This limit destroys all distinction between the charging lines of the two dots and is fundamentally different from the avoidance pattern observed here. We discovered that the latter, with its parallelogram-shaped cells, could be reproduced with $C_m = 0$ by replacing the charge vector in Eq. (2) with the modified form $Q_1 = (N_1 + N_2)e$, $Q_2 = N_2e$; this physically amounts to regarding the outer dot (dot 1) as including the charge of inner dot in its total electron count. The need for such a substitution can be seen from the charge stability diagram [Fig. 5(d)]. Since the condition for charging dot 1 is not changed by crossing the reconfiguration line, the suggestion that it depends on $(N_1 + N_2)$ rather than only N_1 naturally follows. (For details of the modified model and calculations, see Supplemental Material [28]).

To reproduce the transition between the parallelogrammatic and hexagonal cells in the charge stability diagram, the simplest method is to introduce a parameter α such that $Q_1 = (N_1 + \alpha N_2)e$. Then as α decreases from one, the dot 2 charging line appears at the corners of the parallelogram and gradually lengthens, producing the hexagonal shape of Fig. 5(e) at $\alpha = 0.6$. A more detailed exposition of our

modified model is given in the Supplemental Material [28] (Figs. S1–S6). Here α is a phenomenological parameter, and the physical interpretation of the case $\alpha < 1$ is not obvious. Further theoretical work on a microscopic model that captures the interaction and quantum properties of the LL QDs is required to fully understand these results.

V. CONCLUSION

We have constructed edge-free graphene LL QDs by inducing local gating effects in the hBN substrate and applying a magnetic field. These LL QDs are tunable using several different knobs: physical size of the charge pocket, magnetic field strength, back-gate voltage, and tip position. With these knobs we can tune our charge pocket between a single QD and a concentric double-QD system which reveals charging patterns not encountered before, the theory of which requires further development. These results will become increasingly important as the use of scanned probes to make electronically functional nanostructures grows and develops.

ACKNOWLEDGMENTS

We thank Steve Blankenship for technical contributions and Leonid Levitov, Cyprian Lewandowski, and Nicolas Lorente for stimulating discussions. D.W., F.G., and C.G. acknowledge support under the Cooperative Research Agreement between the University of Maryland and the National Institute of Standards and Technology, Grant No. 70NANB10H193, through the University of Maryland. K.W. and T.T. acknowledge support from the Elemental Strategy Initiative conducted by the MEXT, Japan and the CREST(JPMJCR15F3), JST.

APPENDIX: METHODS

The devices were fabricated employing a wet transfer technique described in Ref. [38]. Monolayer graphene and hBN flakes were prepared by mechanical exfoliation onto different substrates where the hBN flake was around 20 nm thick. After transferring, metallic contacts (Cr/Pd/Au) including a set of radial guides for STM navigation were deposited on top of the heterostructure using standard e-beam lithography. Finally, the device was annealed for 5 h in forming gas (5% H₂/95% Ar) at 350°C to remove processing residues. Further annealing of the device at 350°C occurred after introduction to the ultrahigh vacuum (UHV) system.

After loading the device into UHV and annealing, it is transferred into the STM module along with an Ir probe tip, which is part of the cryogenic STM system [39]. The Ir probe tip was prepared by annealing and field-ion evaporation in a field-ion microscope. The probe was optically aligned onto the device guideway using an optical telescope at room temperature. Subsequently, the STM module is lowered into the cryostat and cooled to 4.3 K. All measurements were made at 4.3 K. Differential tunneling conductance measurements, $g(\mathbf{r}, V_B, V_g, B) \equiv dI/dV_B$, were obtained modulating the sample bias, V_B , and using standard lock-in techniques to obtain spectral maps as a function of position \mathbf{r} , V_B , back gate potential, V_g , and magnetic field, B .

The spectral maps in Fig. 1(e), and Figs. 2(a) and 2(b), are shown normalized by the average conductance of each row in the image to enhance the intensity within the graphene phonon gap: $\frac{g(r, V_B)}{\langle g \rangle + \delta}$, where $\delta = 0.02$ nS (see Supplemental

Material [28] for further discussion of the phonon gap, and references [10–13] therein). The other spectral maps, $g(r, V_B)$ and $g(V_g, V_B)$, have a smooth background subtracted to remove the graphene dispersion as described in Ref. [14].

-
- [1] L. P. Kouwenhoven, D. G. Austing, and S. Tarucha, *Rep. Prog. Phys.* **64**, 701 (2001).
- [2] S. M. Reimann and M. Manninen, *Rev. Mod. Phys.* **74**, 1283 (2002).
- [3] T. Hensgens, T. Fujita, L. Janssen, X. Li, C. J. V. Diepen, C. Reichl, W. Wegscheider, S. D. Sarma, and L. M. K. Vandersypen, *Nature* **548**, 70 (2017).
- [4] D. Loss and D. P. DiVincenzo, *Phys. Rev. A* **57**, 120 (1998).
- [5] A. Imamoglu, D. D. Awschalom, G. Burkard, D. P. DiVincenzo, D. Loss, M. Sherwin, and A. Small, *Phys. Rev. Lett.* **83**, 4204 (1999).
- [6] P. E. Allain and J. N. Fuchs, *Eur. Phys. J. B* **83**, 301 (2011).
- [7] M. I. Katsnelson, K. S. Novoselov, and A. K. Geim, *Nat Phys* **2**, 620 (2006).
- [8] G. Giavaras, P. A. Maksym, and M. Roy, *J. Phys.: Condens. Matter* **21**, 102201 (2009).
- [9] G. Giavaras and F. Nori, *Phys. Rev. B* **85**, 165446 (2012).
- [10] N. M. Freitag, L. A. Chizhova, P. Nemes-Incze, C. R. Woods, R. V. Gorbachev, Y. Cao, A. K. Geim, K. S. Novoselov, J. Burgdörfer, F. Libisch, and M. Morgenstern, *Nano Lett.* **16**, 5798 (2016).
- [11] J. Velasco, L. Ju, D. Wong, S. Kahn, J. Lee, H.-Z. Tsai, C. Germany, S. Wickenburg, J. Lu, T. Taniguchi, K. Watanabe, A. Zettl, F. Wang, and M. F. Crommie, *Nano Lett.* **16**, 1620 (2016).
- [12] J. Lee, D. Wong, J. Velasco Jr, J. F. Rodriguez-Nieva, S. Kahn, H.-Z. Tsai, T. Taniguchi, K. Watanabe, A. Zettl, F. Wang, L. S. Levitov, and M. F. Crommie, *Nat. Phys.* **12**, 1032 (2016).
- [13] F. Ghahari, D. Walkup, C. Gutiérrez, J. F. Rodriguez-Nieva, Y. Zhao, J. Wyrick, F. D. Natterer, W. G. Cullen, K. Watanabe, T. Taniguchi, L. S. Levitov, N. B. Zhitenev, and J. A. Stroscio, *Science* **356**, 845 (2017).
- [14] C. Gutiérrez, D. Walkup, F. Ghahari, C. Lewandowski, J. F. Rodriguez-Nieva, K. Watanabe, T. Taniguchi, L. S. Levitov, N. B. Zhitenev, and J. A. Stroscio, *Science* **361**, 789 (2018).
- [15] Y. Zhao, J. Wyrick, F. D. Natterer, J. F. Rodriguez-Nieva, C. Lewandowski, K. Watanabe, T. Taniguchi, L. S. Levitov, N. B. Zhitenev, and J. A. Stroscio, *Science* **348**, 672 (2015).
- [16] C. J. Chen, *J. Vac. Sci. Technol., A* **6**, 319 (1988).
- [17] F. Marczinowski, J. Wiebe, F. Meier, K. Hashimoto, and R. Wiesendanger, *Phys. Rev. B* **77**, 115318 (2008).
- [18] K. Teichmann, M. Wenderoth, S. Loth, R. G. Ulbrich, J. K. Garleff, A. P. Wijnheijmer, and P. M. Koenraad, *Phys. Rev. Lett.* **101**, 076103 (2008).
- [19] V. W. Brar, R. Decker, H.-M. Solowan, Y. Wang, L. Maserati, K. T. Chan, H. Lee, Ç. O. Girit, A. Zettl, S. G. Louie, M. L. Cohen, and M. F. Crommie, *Nat. Phys.* **7**, 43 (2011).
- [20] D. Wong, J. Velasco Jr, L. Ju, J. Lee, S. Kahn, H.-Z. Tsai, C. Germany, T. Taniguchi, K. Watanabe, A. Zettl, F. Wang, and M. F. Crommie, *Nat. Nano* **10**, 949 (2015).
- [21] J. Wyrick, F. D. Natterer, Y. Zhao, K. Watanabe, T. Taniguchi, W. G. Cullen, N. B. Zhitenev, and J. A. Stroscio, *ACS Nano* **10**, 10698 (2016).
- [22] W. G. van der Wiel, S. De Franceschi, J. M. Elzerman, T. Fujisawa, S. Tarucha, and L. P. Kouwenhoven, *Rev. Mod. Phys.* **75**, 1 (2002).
- [23] A. K. Evans, L. I. Glazman, and B. I. Shklovskii, *Phys. Rev. B* **48**, 11120 (1993).
- [24] M. T. Woodside and P. L. McEuen, *Science* **296**, 1098 (2002).
- [25] A. G. F. Garcia, M. König, D. Goldhaber-Gordon, and K. Todd, *Phys. Rev. B* **87**, 085446 (2013).
- [26] Y.-J. Yu, Y. Zhao, S. Ryu, L. E. Brus, K. S. Kim, and P. Kim, *Nano Lett.* **9**, 3430 (2009).
- [27] W. M. H. Sachtler, G. J. H. Dorgelo, and A. A. Holscher, *Sur. Sci.* **5**, 221 (1966).
- [28] See Supplemental Material at <http://link.aps.org/supplemental/10.1103/PhysRevB.101.035428> for supplementary figures, data, and discussion.
- [29] R. Hanson, L. P. Kouwenhoven, J. R. Petta, S. Tarucha, and L. M. K. Vandersypen, *Rev. Mod. Phys.* **79**, 1217 (2007).
- [30] J. M. Thijssen and H. S. J. Van der Zant, *Physica Status Solidi (b)* **245**, 1455 (2008).
- [31] A. H. Castro Neto, F. Guinea, N. M. R. Peres, K. S. Novoselov, and A. K. Geim, *Rev. Mod. Phys.* **81**, 109 (2009).
- [32] N. M. Freitag, T. Reisch, L. A. Chizhova, P. Nemes-Incze, C. Holl, C. R. Woods, R. V. Gorbachev, Y. Cao, A. K. Geim, K. S. Novoselov, J. Burgdörfer, F. Libisch, and M. Morgenstern, *Nature Nanotech.* **13**, 392 (2018).
- [33] J. R. Petta, A. C. Johnson, C. M. Marcus, M. P. Hanson, and A. C. Gossard, *Phys. Rev. Lett.* **93**, 186802 (2004).
- [34] D. Schröer, A. D. Greentree, L. Gaudreau, K. Eberl, L. C. L. Hollenberg, J. P. Kotthaus, and S. Ludwig, *Phys. Rev. B* **76**, 075306 (2007).
- [35] F. R. Waugh, M. J. Berry, D. J. Mar, R. M. Westervelt, K. L. Campman, and A. C. Gossard, *Phys. Rev. Lett.* **75**, 705 (1995).
- [36] J. M. Golden and B. I. Halperin, *Phys. Rev. B* **53**, 3893 (1996).
- [37] C. Livermore, C. H. Crouch, R. M. Westervelt, K. L. Campman, and A. C. Gossard, *Science* **274**, 1332 (1996).
- [38] C. R. Dean, A. F. Young, I. Meric, C. Lee, L. Wang, S. Sorgenfrei, K. Watanabe, T. Taniguchi, P. Kim, K. L. Shepard, and J. Hone, *Nat. Nano* **5**, 722 (2010).
- [39] R. J. Celotta, S. B. Balakirsky, A. P. Fein, F. M. Hess, G. M. Rutter, and J. A. Stroscio, *Rev. Sci. Instrum.* **85**, 121301 (2014).